



Superionic iron oxide–hydroxide in Earth’s deep mantle

HPSTAR
1108-2021

Mingqiang Hou^{1,2,14}, Yu He^{3,14}, Bo Gyu Jang^{1,4}, Shichuan Sun³, Yukai Zhuang¹, Liwei Deng⁵, Ruilian Tang^{1,6}, Jiuhua Chen⁷, Feng Ke⁸, Yue Meng⁹, Vitali B. Prakapenka¹⁰, Bin Chen¹, Ji Hoon Shim⁴, Jin Liu¹✉, Duck Young Kim¹✉, Qingyang Hu¹✉, Chris J. Pickard^{11,12}, Richard J. Needs¹³ and Ho-Kwang Mao¹

Water ice becomes a superionic phase under the high pressure and temperature conditions of deep planetary interiors of ice planets such as Neptune and Uranus, which affects interior structures and generates magnetic fields. The solid Earth, however, contains only hydrous minerals with a negligible amount of ice. Here we combine high pressure and temperature electrical conductivity experiments, Raman spectroscopy and first-principles simulations to investigate the state of hydrogen in the pyrite-type FeO_2H_x ($x \leq 1$), which is a potential H-bearing phase near the core-mantle boundary. We find that when the pressure increases beyond 73 GPa at room temperature, symmetric hydroxyl bonds are softened and the H^+ (or proton) becomes diffusive within the vicinity of its crystallographic site. Increasing temperature under pressure, the diffusivity of hydrogen is extended beyond the individual unit cell to cover the entire solid, and the electrical conductivity soars, indicating a transition to the superionic state, which is characterized by freely moving protons and a solid FeO_2 lattice. The highly diffusive hydrogen provides fresh transport mechanisms for charge and mass, which dictate the geophysical behaviours of electrical conductivity and magnetism, as well as geochemical processes of redox, hydrogen circulation and hydrogen isotopic mixing in Earth’s deep mantle.

Hydrogen plays an important role in the deep interior of the Earth^{1,2}, where its mobility and bonding properties are altered dramatically from localized to globally itinerant with increasing depth. At shallower depths, hydrogen bonds with oxygen, the most abundant element in Earth, to form hydroxyls that modulate the electrical^{3,4}, thermal⁵ and elastic⁶ properties of the host minerals and dictate redox, melting and isotope partitioning⁷. Properties of hydroxyl groups have been extensively studied during the past half century as a means to locate deep-water reservoirs and to monitor water circulation for a broad range of applications in interpretation of large geophysical and geochemical features in depth^{8–10}. Hydroxyl starts with an asymmetric configuration $\text{O}-\text{H}\cdots\text{O}$ in which the hydrogen atom between two oxygen atoms is bonded to one oxygen atom by a strong, short covalent bond ($\text{O}-\text{H}$) and to the other oxygen atom on the opposite side by a weak, long hydrogen bond ($\text{H}\cdots\text{O}$). With increasing depth and pressure (P), the covalent bonds of hydroxyl are lengthened and the hydrogen bonds are shortened until the two bond lengths become equal, with H reaching the symmetrical centre of the two adjacent oxygen atoms. The symmetrization of hydroxyl bonding was observed in H_2O ice VII to ice X transition at 60 GPa and room temperature (T)¹¹. Theory further predicted that at high T , the H^+ (proton)

becomes itinerant in the ice crystal lattice and moves freely like a fluid within a framework of oxygen, reaching the superionic state¹². The challenging experiments of superionic ice have been actively pursued during the past two decades^{12,13} and observed very recently with nanosecond X-ray diffraction (XRD) in laser-shocked high P – T experiments^{14,15}.

Up to now, the exotic superionic state has been considered only for pure H_2O ice X, which is a minor phase in the Earth’s deep interior. Hydrogen in the deep Earth is mostly hidden in hydrous minerals. In this article, we investigate further P – T effects beyond symmetrization and report the observations of new ‘relaxation’ and superionic states that the protons are liberated from their localized bonded states and become highly diffusive, moving freely throughout the host phase. The dramatic changes of the fundamental bonding nature and mobility mandate a re-evaluation of the role of hydrogen in the deep Earth.

We initiate the research by focusing our investigation on the newly discovered pyrite (Py) type FeO_2H_x ($x \leq 1$), which is a candidate hydrogen-bearing phase in the core–mantle boundary (CMB)^{16–19}. FeO_2H_x ($x \leq 1$) has the same Py-type structure as FeO_2 but features an expanded volume due to the incorporation of H. Previous experiments exhibit a range of x from 0.4 to 1.0 for

¹Center for High Pressure Science and Technology Advanced Research (HPSTAR), Beijing, China. ²Institute of Meteoritics, Department of Earth and Planetary Sciences, University of New Mexico, Albuquerque, NM, USA. ³Key Laboratory of High-Temperature and High-Pressure Study of the Earth’s Interior, Institute of Geochemistry, Chinese Academy of Sciences, Guiyang, China. ⁴Department of Chemistry, Pohang University of Science and Technology, Pohang, Korea. ⁵College of New Materials and New Energies, Shenzhen Technology University, Guangdong, China. ⁶School of Materials Science and Engineering, Changchun University of Science and Technology, Changchun, China. ⁷Center for Study of Matter under Extreme Conditions, Department of Mechanical and Materials Engineering, Florida International University, Miami, FL, USA. ⁸Department of Geological Sciences, Stanford University, Stanford, CA, USA. ⁹High Pressure Collaborative Access Team, X-ray Science Division, Argonne National Laboratory, Argonne, IL, USA. ¹⁰Center for Advanced Radiation Sources, University of Chicago, Chicago, IL, USA. ¹¹Department of Materials Science and Metallurgy, University of Cambridge, Cambridge, UK. ¹²Advanced Institute for Materials Research, Tohoku University, Aoba, Sendai, Japan. ¹³Theory of Condensed Matter Group, Cavendish Laboratory, Cambridge, UK. ¹⁴These authors contributed equally: Mingqiang Hou, Yu He. ✉e-mail: jin.liu@hpstar.ac.cn; duckyoung.kim@hpstar.ac.cn; qingyang.hu@hpstar.ac.cn

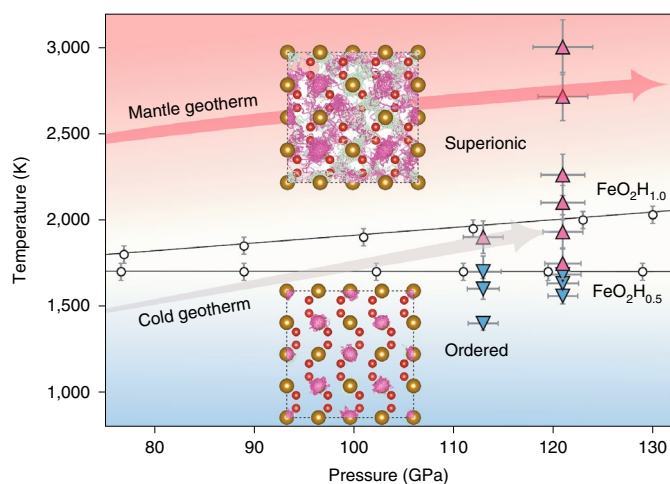


Fig. 1 | P–T phase diagram for ordered to superionic FeO_2H_x . Open circles are data points in the FPMD simulation. Error bars are statistic perturbations of T in each simulation. Uncertainty of P is within ± 2 GPa. Upward and downward triangles represent the superionic and ordered phases, respectively, on the basis of EC measurements. Inset figures are the crystal lattice of FeO_2 with diffusive H (purple and green clouds represent different H layers).

FeO_2H_x (Extended Data Fig. 1). Synthesized above 75 GPa, the H in Py- FeO_2H_x is already in the symmetric position (Extended Data Fig. 2). Using first-principles computations and electrical conductivity (EC), XRD and Raman spectroscopic measurements in a diamond-anvil cell (DAC) over a P – T range pertinent to the deep lower mantle (DLM), we observed not only the superionic state in Py- FeO_2H_x above 1,800 K and 121 GPa, but also a previously unknown intermediate bond-softening transition. The superionic proton conduction induces remarkable increases in the charge and mass transport that greatly impact the geophysical and geochemical processes in the DLM and particularly near the CMB.

Superionic FeO_2H_x from first-principles calculation

We study the superionic state of the Py- FeO_2H_x by first-principles molecular dynamics (FPMD) calculations and predict the phase boundary of ordered crystalline and the superionic phase (Fig. 1 and Methods). We track the motions of atoms in the Py- FeO_2H_x ($x=1$ and 0.5) supercell at 1,500–3,300 K and 80–140 GPa. The length of each simulation is equivalent to 10 picoseconds (ps). During initial heating, localized H diffusion is observed even at relatively low temperatures, and the movements of protons are described by small mean-square displacement (MSD) values and low diffusion coefficients D_{H} (Extended Data Figs. 3 and 4). With further heating (for example, 2,000 K and 80 GPa), the protons start to become unbounded with a finite degree of localization, which is signified by the monotonical increment of MSD with simulation time and sudden improvement of D_{H} (Extended Data Fig. 4). The liquid-like motion of H^+ in the solid FeO_2 lattice suggests that Py- FeO_2H_x enters a superionic state above 2,000 K at 80–130 GPa. The proton diffusivity further increases with T , and eventually, H^+ is delocalized from the O–H–O triplet, promoting to the so-called delocalized superionic phase with even faster proton diffusion²⁰. On the basis of our FPMD simulation, the Py- FeO_2H_x is predicted to enter the superionic state above $\sim 1,700$ K from 80–130 GPa that covers even the coldest DLM geotherm (Fig. 1).

The O–H bonding in FeO_2H_x

The consequence of superionic state is multifold. Delocalized H atoms break hydroxyl bonding, a signature of hydrous minerals.

Although it is technically challenging to recognize the motion of H atoms by experiment, the evolution of O–H bonding is sensitive to Raman spectroscopy. We collected the Raman spectra of Py- FeO_2H_x at room T after it was synthesized at 2,200 K and 94 GPa and decompressed to 51 GPa (Fig. 2). Below 73 GPa, the stiffening of O–H stretching mode around $3,500\text{ cm}^{-1}$ is consistent with the symmetric O–H–O bonds (Extended Data Fig. 2). However, above 73 GPa, the same mode softens precipitously, indicating the enhancement of H^+ mobility. The intensity of the O–H Raman peak is also weakened by approximately 55%. The observations are consistent with our FPMD simulation, which shows that protons are activated and diffuse locally, thus weakening the symmetric O–H–O bonds. The restrained diffusion of H^+ in the Py- FeO_2H_x at high P , low T can be described by a relaxation state, which is regarded as a low- T precursor of superionic state; high T is needed to increase the mobility beyond the unit-cell level.

Observations of superionic state by EC measurement

In the superionic state, the intensities of the Raman signal from the O–H bonds will be greatly reduced and no longer be an effective probe. However, EC (σ), which is the sum of FeO_2 lattice electron mobility (EM) and ionic conductivity (IC), provides the diagnostic of mobile H^+ :

$$\sigma = \sigma_{\text{EM}} + \sigma_{\text{IC}} \quad (1)$$

The contribution of σ_{IC} directly relates to the mobility of H^+ , while σ_{EM} stems mainly from electron–phonon (e -ph) and electron–electron (e - e) scattering in the FeO_2 lattice (Methods). We calculated the IC in the predicted superionic regime by following the Nernst–Einstein equation (Methods). In Fig. 3a–c, the IC from the proton is on the order of $10^{2.5}$ – $10^{3.0}\text{ S m}^{-1}$ at $\sim 3,000$ K and further boosted in the presence of an electrical field²¹. While IC is negligible compared with EM at low T , the delocalized superionic state will substantially boost the IC, which will make a detectable contribution to the total EC.

We then conducted in situ four-probe EC measurements on the Py- FeO_2H_x . The sample was initially synthesized at 113 GPa by laser heating for one hour, and the EC experiment was performed at 121 GPa during a heating cycle up to 3,300 (± 200) K (Methods). Note that the hydrogen content x and the chemical composition of the sample are well kept before and after the EC experiment run, checking by high- P XRD (Extended Data Figs. 5 and 6). In Fig. 3c, a kink with σ surging by a factor of two was observed around 1,800–2,000 K. This is well explained by the onset of the superionic proton conduction mechanism. Here, we included the effects of induced electrical field (Methods) and estimated the contribution of IC from first-principles calculations in the full T range. The IC contribution accounted for roughly one-third of the total EC and plateaued above $\sim 2,400$ K, which might be due to the saturation of both IC and EM (Fig. 3c). This observation indicates the total EC of Py- FeO_2H_x is of the same order as 10^4 S m^{-1} , exceeding the EC values of all known anhydrous lower-mantle minerals, including bridgmanite (Brg)^{22,23}, post-perovskite (PPv)²² and ferropericlaite (Fp)²⁴ by at least two orders of magnitude at CMB conditions (Table 1). Note that the high EC of Py- FeO_2H_x is still several orders of magnitude lower than that of metals using the same experimental scheme²⁵, and its positive correlation with increasing T is opposite to metals.

Implications of H behaviours in Earth's interior

The observed transitions from hydroxyl O–H to highly diffusive H in oxides lead to paradigm changes in hydrogen cycles¹⁶ and reservoirs²⁶ in the DLM. First, all previous implications related to hydration in Earth's interior would be enhanced in the DLM. For example, the long-period electromagnetic data from length-of-day series and geophysical–geomagnetic measurements [C-responses²⁷] combined

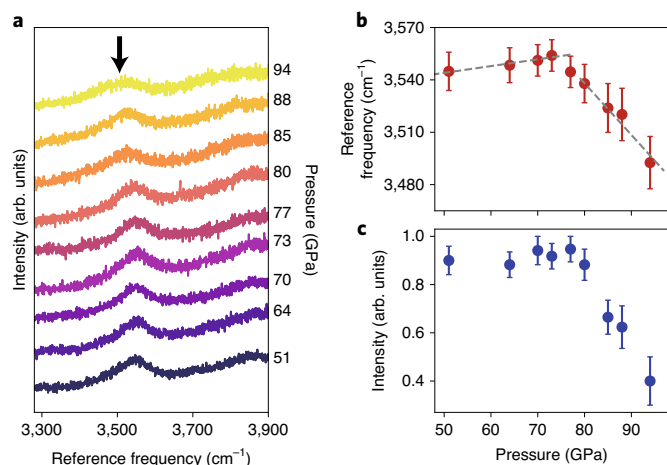


Fig. 2 | Raman spectra of a decompressed Py-FeO₂H_x sample. a, Evolution of the Raman spectrum by decompressing a Py-FeO₂H_x sample from 94 GPa. The black arrow denotes the O-H Raman mode. Colour gradient represents the change of P . **b, c**, Change of O-H mode position and intensity. The modes become softened from 77 to 94 GPa. Error bars are derived from Gaussian-type peak fitting. The P medium was Ar. Uncertainty of P is ± 2 GPa.

with laboratory high P - T EC data of lower-mantle minerals have provided a powerful constraint on the thermo-chemical structure of the lower mantle²⁸. The unusually high EC and the positive correlation between T and EC for superionic Py-FeO₂H_x enhance the possibility of separating the thermal and hydration effects. They will eventually help to detect hydrogen and oxygen reservoirs previously proposed for the ultralow velocity zone on the basis of elasticity measurements²⁹. The high EC and superionic mass transport might also contribute substantially to deep mantle thermal conductivity³⁰. Thorough mineral physical investigations of the superionic phases would furnish a comprehensive geophysical insight into the enigmatic D'' layer.

Moreover, superionic Py-FeO₂H_x introduces a new geochemical scenario that has rarely been considered before. The Earth's interior was thought to consist of either solid minerals that were immobile and only reached local chemical equilibrium or fluids that were mobile and promoted equilibrium over an extended region. Superionic Py-FeO₂H_x is a new type of solid consisting of fluid-like mobile H⁺ diffusing freely in the lattice framework of oxygen and other cations. Unlike the upper mantle, in which the regional geochemistry is dictated by the oxygen fugacity and redox state, the DLM geochemistry would be characteristic of the regional homogeneous hydrogen fugacity and heterogeneous redox states. The integer hydrogen stoichiometry in low- P hydrous minerals, such as α - and ϵ -FeO₂H, shifts to a fraction, such as the Py-FeO₂H_x in the superionic region. Hydrogen fugacity may become a measurement of geochemistry in the superionic regions, where a very unusual oxygen stoichiometry³¹, and distinct redox state, may appear^{32,33}. Superionic proton conduction introduces a mass transport mechanism, which also raises intriguing insights into the hydrogen isotope geochemistry of the deep Earth. The δD values collected from mantle-derived rocks retain many geochemical signatures of Earth's deep-water cycles. Assessment of D/H isotopic fractionation from oceanic basalts indicates that δD is generally homogeneous (with $\delta D = -60 \pm 5\%$ compared with Standard Mean Ocean Water)³⁴ after removing seawater contamination. Rapid mass transport and isotope exchange by H and D diffusion could be one of the controlling factors at these depths.

The stability of FeO₂H_x, either partially ($x < 1$) or fully ($x = 1$) hydrogenated, has been well established experimentally by at least

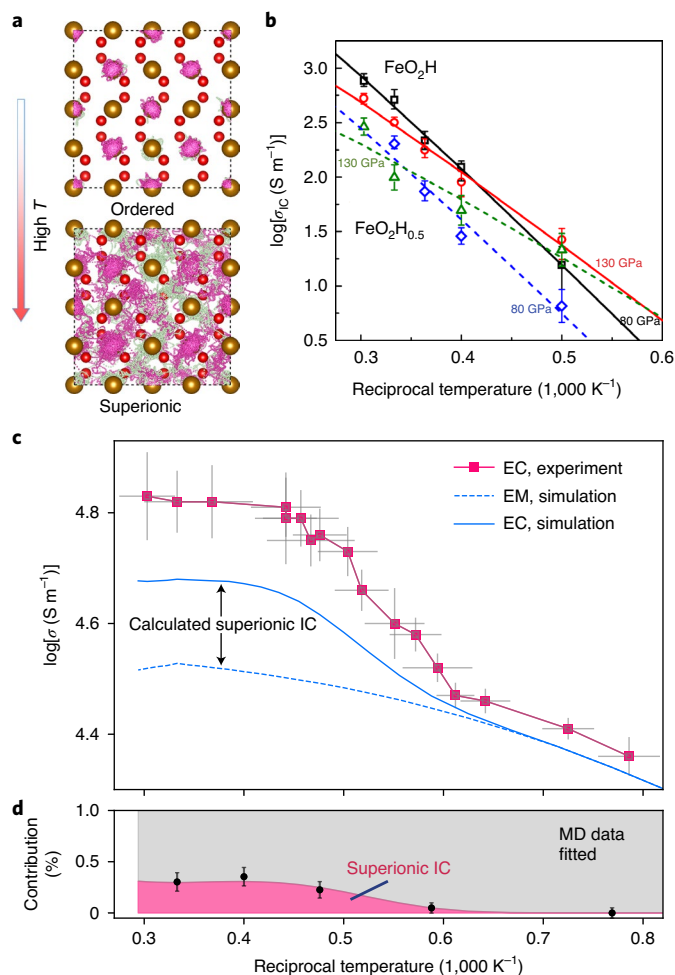


Fig. 3 | Superionic transition in Py-FeO₂H_x. a, The evolution of proton trajectories of FeO₂H_{0.5} from the solid to superionic state. Trajectories with different colours represent different H layers. **b**, Calculated IC of FeO₂H and FeO₂H_{0.5}. Black, red, blue and green symbols represent IC of FeO₂H at 80 GPa, FeO₂H at 130 GPa, FeO₂H_{0.5} at 80 GPa and FeO₂H_{0.5} at 130 GPa, respectively. **c**, Total EC at 121 GPa upon laser heating. Errors were calculated and propagated on the basis of fluctuations in experimental conditions, with details in the Methods. Experiment is compared with simulation (blue curve), which summed up values of calculated EM (dashed line) and IC under a static electrical field along the [100] direction. **d**, Theoretical calculation predicts IC makes approximately one-third of total EC in the superionic state. Errors were estimated from the FPMD trajectories. MD, molecular dynamics.

four research groups^{16–19,35}. Superionic FeO₂H_x is a stable minor phase along the relative cold deep subduction slabs (Fig. 1)³⁶. The superionization depends mainly on the combined P - T effects on the H⁺ mobility in oxygen sublattices. Note that the Py-FeO₂H_x is just the first example of superionic phases in the DLM. Very likely, hydrogen in the recently discovered dense hydrogen-bearing oxides that are stable under the DLM's high P - T conditions, such as dense hydrous phases, may also exhibit superionic behaviour. We are facing a new and refreshing view of DLM geophysics and geochemistry with answers lying in extensive mineral physics investigations of their superionicity.

Experimental methodology

The multiple requirements of sample synthesis, hydrogen containment, conductivity measurements and in situ sample and hydrogen

Table 1 | EC values of mantle materials

Material	<i>P</i> (GPa)	<i>T</i> (K)	EC (S m ⁻¹)
(Mg _{0.9} ,Fe _{0.1})SiO ₃ , Brg ²²	117	2,660	3 × 10 ⁻²
Pyrolite ⁴³	129	2,000	1.5 × 10 ¹
Mg _{0.83} Fe _{0.21} Al _{0.06} Si _{0.91} O ₃ , Brg ²³	82	2,000	7.1 × 10 ¹
(Mg _{0.9} ,Fe _{0.1})SiO ₃ , PPv ²²	143	3,000	1.4 × 10 ²
(Mg _{0.817} ,Fe _{0.19})O, Fp ²⁴	116	2,000	3.5 × 10 ²
(Mg _{0.817} ,Fe _{0.19})O, Fp ²⁴	131	2,730	5.5 × 10 ²
MORB ⁴³	133	3,000	5.6 × 10 ²
Py-FeO₂H_x (this study)	121	3,000	6.6(5) × 10⁴
FeO wüstite ⁴⁴	135	3,700	9.0 × 10 ⁴

Values were taken at various *P* and *T* in the ascending EC values. The EC of Py-FeO₂H_x is of the same order as metallic FeO at CMB conditions.

characterization under the extreme *P*–*T* conditions would normally present a great challenge. Fortunately, such techniques have already been well developed and perfected during the past two decades due to the similar, but more stringent, experimental requirements in the quests of metallic hydrogen and room-*T* superconductors up to 400 GPa. Some very recent examples include the breakthrough of near room-*T* superconductivity of hydrogen-rich systems synthesized with or without laser heating above 200 GPa (refs. ^{37,38}), and semimetallic transition of hydrogen at 380 GPa (ref. ³⁹) using the four-probe method and *c*-BN insulating gasket as in the present work, and x-ray crystallography of hydrogen phase III using *c*-BN as a low-background gasket up to 254 GPa (ref. ⁴⁰). It has been established that *c*-BN gasket can reliably seal bulk hydrogen with a small amount of hydrogen lost by infiltrating into the gasket. Using this matured ultrahigh-*P* technology, our present experiment at much lower *P*s (~120 GPa) is quite robust.

Our experiments consist of two stages. During the first synthesis stage, the solid goethite sample and four electric leads were loaded in *c*-BN/Re double gasket, compressed to 113 GPa and heated to 2,000 K for approximately 1 hour to ensure complete conversion to Py-FeO₂H_x. At room *T* under *P*, we scanned the sample with Raman probe but could not find any sign of the H₂ vibron, presumably the liberated H₂ infiltrating through the *c*-BN gasket and being sealed by the outer Re gasket⁴¹. During our second-stage experiment, the sample assemblage was laser-heated again with simultaneous EC measurement (Fig. 3c). We took XRD patterns before and after the EC experiment (Extended Data Figs. 5 and 6) and confirmed that the sample remained stable as Py-FeO₂H with *x* fixed to the maximum stoichiometry allowed by the structure, that is, 0.87(8) in the present work (Methods).

The maximum amount of fluid hydrogen released to form FeO₂H_{0.86} is approximately 0.5–2 vol% of the solid volume. Because our Raman detection limit is 0.2% H₂, most H₂ is expected to be lost through the *c*-BN gasket. However, combining XRD and Raman scanning, we are confident that there is no obvious escape of H₂ in the EC experiment run, which means our data in Fig. 3 were reproduced under a chemically stable environment. Our experimental results suggest the surge of EC occurs between 1,700 and 1,800 K and at 121 GPa. At the corresponding *P*–*T* conditions, the EC of fluid H₂ or superionic H₂O is below that of FeO₂H_x (ref. ⁴² and Extended Data Fig. 7). Therefore, even if a small amount of H₂ or H₂O alloyed with the FeO₂H_x sample, the EC of the sample is unlikely to be enhanced (Extended Data Figs. 8 and 9).

Online content

Any methods, additional references, Nature Research reporting summaries, source data, extended data, supplementary information,

acknowledgements, peer review information; details of author contributions and competing interests; and statements of data and code availability are available at <https://doi.org/10.1038/s41561-021-00696-2>.

Received: 14 February 2020; Accepted: 19 January 2021;

Published online: 8 March 2021

References

- Pamato, M. G. et al. Lower-mantle water reservoir implied by the extreme stability of a hydrous aluminosilicate. *Nat. Geosci.* **8**, 75–79 (2014).
- Schmandt, B., Jacobsen, S. D., Becker, T. W., Liu, Z. & Dueker, K. G. Dehydration melting at the top of the lower mantle. *Science* **344**, 1265–1268 (2014).
- Wang, D., Mookherjee, M., Xu, Y. & Karato, S.-I. The effect of water on the electrical conductivity of olivine. *Nature* **443**, 977–980 (2006).
- Yoshino, T. & Katsura, T. Electrical conductivity of mantle minerals: role of water in conductivity anomalies. *Annu. Rev. Earth Planet. Sci.* **41**, 605–628 (2013).
- Chang, Y.-Y., Hsieh, W.-P., Tan, E. & Chen, J. Hydration-reduced lattice thermal conductivity of olivine in Earth's upper mantle. *Proc. Natl Acad. Sci. USA* **114**, 4078–4081 (2017).
- Mao, Z. et al. Velocity crossover between hydrous and anhydrous forsterite at high pressures. *Earth Planet. Sci. Lett.* **293**, 250–258 (2010).
- Litasov, K. D. & Ohtani, E. in *Advances in High-Pressure Mineralogy* Special Paper 421 (ed. Ohtani, E.) 115–156 (Geological Society of America, 2007).
- Hirschmann, M. M. Water, melting, and the deep Earth H₂O cycle. *Annu. Rev. Earth Planet. Sci.* **34**, 629–653 (2006).
- Jacobsen, S. D. & van der Lee, S. *Earth's Deep Water Cycle* Volume 168 (American Geophysical Union, 2006).
- Ni, H. et al. Distribution, cycling and impact of water in the Earth's interior. *Natl Sci. Rev.* **4**, 879–891 (2017).
- Goncharov, A. F., Struzhkin, V. V., Somayazulu, M., Hemley, R. J. & Mao, H. K. Compression of ice to 210 GPa: evidence for a symmetric hydrogen bonded phase. *Science* **273**, 218–220 (1996).
- Cavazzoni, C. et al. Superionic and metallic states of water and ammonia at giant planet conditions. *Science* **283**, 44–46 (1999).
- Sugimura, E. et al. Experimental evidence of superionic conduction in H₂O ice. *J. Chem. Phys.* **137**, 194505 (2012).
- Millot, M. et al. Experimental evidence for superionic water ice using shock compression. *Nat. Phys.* **14**, 297–302 (2018).
- Millot, M. et al. Nanosecond X-ray diffraction of shock-compressed superionic water ice. *Nature* **569**, 251–255 (2019).
- Hu, Q. et al. Dehydrogenation of goethite in Earth's deep lower mantle. *Proc. Natl Acad. Sci. USA* **114**, 1498–1501 (2017).
- Nishi, M., Kuwayama, Y., Tsuchiya, J. & Tsuchiya, T. The pyrite-type high-pressure form of FeOOH. *Nature* **547**, 205–208 (2017).
- Boulevard, E. et al. CO₂-induced destabilization of pyrite-structured FeO₂H_x in the lower mantle. *Natl Sci. Rev.* **5**, 870–877 (2018).
- Yuan, L. et al. Chemical reactions between Fe and H₂O up to megabar pressures and implications for water storage in the Earth's mantle and core. *Geophys. Res. Lett.* **45**, 1330–1338 (2018).
- Hernandez, J.-A. & Caracas, R. Superionic–superionic phase transitions in body-centered cubic H₂O ice. *Phys. Rev. Lett.* **117**, 135503 (2016).
- Futera, Z., Tse, J. S. & English, N. J. Possibility of realizing superionic ice VII in external electric fields of planetary bodies. *Sci. Adv.* **6**, eaaz2915 (2020).
- Ohta, K. et al. The electrical conductivity of post-perovskite in Earth's D' layer. *Science* **320**, 89–91 (2008).
- Sinmyo, R., Pesce, G., Greenberg, E., McCammon, C. & Dubrovinsky, L. Lower mantle electrical conductivity based on measurements of Al, Fe-bearing perovskite under lower mantle conditions. *Earth Planet. Sci. Lett.* **393**, 165–172 (2014).
- Ohta, K., Yagi, T., Hirose, K. & Ohishi, Y. Thermal conductivity of ferropericlase in the Earth's lower mantle. *Earth Planet. Sci. Lett.* **465**, 29–37 (2017).
- Zhang, Y. et al. Reconciliation of experiments and theory on transport properties of iron and the geodynamo. *Phys. Rev. Lett.* **125**, 078501 (2020).
- Mao, H.-K. et al. When water meets iron at Earth's core–mantle boundary. *Natl Sci. Rev.* **4**, 870–878 (2017).
- Khan, A. & Shankland, T. J. A geophysical perspective on mantle water content and melting: inverting electromagnetic sounding data using laboratory-based electrical conductivity profiles. *Earth Planet. Sci. Lett.* **317–318**, 27–43 (2012).
- Deschamps, F. & Khan, A. Electrical conductivity as a constraint on lower mantle thermo-chemical structure. *Earth Planet. Sci. Lett.* **450**, 108–119 (2016).
- Liu, J. et al. Hydrogen-bearing iron peroxide and the origin of ultralow-velocity zones. *Nature* **551**, 494–497 (2017).

30. Hsieh, W.-P., Deschamps, F., Okuchi, T. & Lin, J.-F. Effects of iron on the lattice thermal conductivity of Earth's deep mantle and implications for mantle dynamics. *Proc. Natl Acad. Sci. USA* **115**, 4099–4104 (2018).
31. Liu, J. et al. Altered chemistry of oxygen and iron under deep Earth conditions. *Nat. Commun.* **10**, 153 (2019).
32. McCammon, C. The paradox of mantle redox. *Science* **308**, 807–808 (2005).
33. Stagno, V., Ojwang, D. O., McCammon, C. A. & Frost, D. J. The oxidation state of the mantle and the extraction of carbon from Earth's interior. *Nature* **493**, 84–88 (2013).
34. Clog, M., Auband, C., Cartigny, P. & Dosso, L. The hydrogen isotopic compositions and water content of southern Pacific MORB: a reassessment of D/H ratio of the depleted mantle reservoir. *Earth Planet. Sci. Lett.* **381**, 156–165 (2013).
35. Boulard, E. et al. Ferrous iron under oxygen-rich conditions in the deep mantle. *Geophys. Res. Lett.* **46**, 1348–1356 (2019).
36. Yoshino, T., Baker, E. & Duffey, K. Fate of water in subducted hydrous sediments deduced from stability fields of FeOOH and AlOOH up to 20 GPa. *Phys. Earth Planet. Inter.* **294**, 106295 (2019).
37. Struzhkin, V. et al. Superconductivity in La and Y hydrides: remaining questions to experiment and theory. *Matter Radiat. Extremes* **5**, 028201 (2020).
38. Snider, E. et al. Room-temperature superconductivity in a carbonaceous sulfur hydride. *Nature* **586**, 373–377 (2020).
39. Eremets, M. I., Drozdov, A. P., Kong, P. P. & Wang, H. Semimetallic molecular hydrogen at pressure above 350 GPa. *Nat. Phys.* **15**, 1246–1249 (2019).
40. Ji, C. et al. Crystallography of low Z material at ultrahigh pressure: case study on solid hydrogen. *Matter Radiat. Extremes* **5**, 038401 (2020).
41. Gregoryanz, E. et al. Everything you always wanted to know about metallic hydrogen but were afraid to ask. *Matter Radiat. Extremes* **5**, 038101 (2020).
42. Weir, S. T., Mitchell, A. C. & Nellis, W. J. Metallization of fluid molecular hydrogen at 140 GPa (1.4 Mbar). *Phys. Rev. Lett.* **76**, 1860–1863 (1996).
43. Ohta, K. et al. Electrical conductivities of pyrolitic mantle and MORB materials up to the lowermost mantle conditions. *Earth Planet. Sci. Lett.* **289**, 497–502 (2010).
44. Ohta, K. et al. Experimental and theoretical evidence for pressure-induced metallization in FeO with rocksalt-type structure. *Phys. Rev. Lett.* **108**, 026403 (2012).

Publisher's note Springer Nature remains neutral with regard to jurisdictional claims in published maps and institutional affiliations.

© The Author(s), under exclusive licence to Springer Nature Limited 2021

Methods

Simulation. Theoretical structure optimization. To calculate the EC of FeO_2H_x , we first optimized the pyrite-type structure of FeO_2H_x to the target P of 120 GPa under the framework of density functional theory. Using the Vienna Ab initio Simulation Package (VASP), the structural optimization was performed by employing the generalized gradient approximation functionals, in particular the Perdew–Burke–Ernzerhof exchange–correlation functional⁴⁵. We treated eight electrons (six in $3d$ and two in $4s$) of Fe, six electrons (two $2s$ and four $2p$) of oxygen, and one s electron of hydrogen as valence electrons explicitly. A plane-wave basis set cut-off energy of 1,000 eV and k -point sampling of 0.06 \AA^{-1} were used. The geometry was optimized until the interatomic force was less than 0.01 eV \AA^{-1} . The optimized structure will be further applied to FPMD simulation, dynamical mean-field theory calculation and FPMD simulation under external electric field.

FPMD simulation. FPMD simulations were performed using the VASP package⁴⁶ and an increased cut-off energy of 800 eV. We used the same Perdew–Burke–Ernzerhof functional as was implemented for structural relaxation. A single gamma point was adopted for k -points sampling in FPMD. H vacancies in $\text{Py-FeO}_2\text{H}_x$ ($x=0.5$) were generated by removing H atoms from a large supercell of $\text{Py-FeO}_2\text{H}$ comprising $2 \times 2 \times 2$ conventional unit cells. FPMD simulation becomes equilibrated after 2 ps at the target P – T with a constant number of atoms, volume and T ensemble. Trajectories of the atomic motions were taken thereafter, with 1 fs time step, and the total time of simulation was equivalent to 10 ps. T was controlled by a Nosé–Hoover thermostat⁴⁷. This computational scheme was tested on superionic ice, and the results are consistent with previous studies (Extended Data Fig. 7).

The velocity autocorrelation function $C_{vv}(t)$ in Extended Data Fig. 2 was calculated on the basis of our FPMD data through the following relation⁴⁸:

$$C_{vv}(t) = \frac{1}{3N} \sum_{\alpha=1}^N w_{\text{H}} \langle v_{\text{H}}(0) \cdot v_{\text{H}}(t) \rangle$$

where $\langle v_{\text{H}}(0) \cdot v_{\text{H}}(t) \rangle$ denotes the averaged value of the scalar products $v_{\text{H}}(0) \cdot v_{\text{H}}(t)$ for atom velocities, w_{H} is the weight coefficient of H ions, t is the time and N is the number of H ions in a supercell. The vibrational density of states is calculated as the Fourier transform of the velocity autocorrelation functions.

Diffusion analysis. To calculate the proton diffusion coefficient, we performed FPMD simulations using a $2 \times 2 \times 2$ supercell for $\text{Py-FeO}_2\text{H}_x$. Note that using a larger supercell does not change the simulation results. The simulations used the canonical ensemble with a time step of 1 fs, with the simulations lasting 7 and 15 ps at temperatures from 1,500 to 3,500 K. This approach is suitable for evaluating the activation enthalpy of ion migration and identifying the ion transport mechanism. To study superionic transport rigorously, we calculated the diffusion coefficient for proton transport and the MSD of the ionic positions. The diffusion coefficient is defined as

$$D = \lim_{d \rightarrow \infty} \left[\frac{1}{2dt} \langle [\tilde{r}(t)]^2 \rangle \right]$$

where d is the dimension of the lattice on which ion hopping takes place. The MSD

$$\langle [\tilde{r}(t)]^2 \rangle = \frac{1}{N} \sum_{i=1}^N \langle [\vec{r}_i(t + t_0) - \vec{r}_i(t_0)]^2 \rangle$$

is averaged over all protons, and $\vec{r}_i(t)$ is the displacement of the i th proton at time t and N is the total number of protons in the system. In practice, the value of D obtained at various temperatures can be fitted with an Arrhenius equation:

$$D = A \exp \left(\frac{-\Delta H}{kT} \right),$$

where ΔH is the activation enthalpy, A is a pre-exponential factor, k is the Boltzmann constant and T is the temperature. The EC was calculated using the diffusion coefficients and the Nernst–Einstein equation:

$$\sigma = \frac{fDcq^2}{kT}$$

in which σ is the EC, f is a numerical factor approximately equal to unity, c is the proton concentration, q is the electrical charge of proton, k is the Boltzmann constant and T is the temperature. Although this approach is a widely used approximation, it is also known to underestimate IC, for example, by a factor of one-third in superionic H_2O (ref. ⁴⁹). In superionic FeO_2H , the Fe ions can change their valance states during proton conduction; thus, it is valuable to consider the polarization effect to predict the IC more accurately. Therefore, our calculated IC is likely to stand on the lower bound.

We also calculated the proton diffusion coefficients D_{H} as a function of T (Extended Data Fig. 4). The change in proton diffusion coefficient is continuous over the P – T region we have studied. The relation between diffusion coefficient and T still obeys the Arrhenius relation as mentioned previously.

Hydrogen diffusion under static electric field. Simulation under a static electric field is to explain IC values in an induced ionic current with the superionic state. Note

that the original proton diffusion rate (without electric field) still applies to the scenario in Earth's deep interior as a global electrical field is unlikely to be sustained in the Earth. FPMD under an external electrical field was conducted in CP2K⁵⁰. We used the same Perdew–Burke–Ernzerhof functionals for the exchange–correlation part of the Hamiltonian and employed the double-zeta valence basis set optimized for the Goedecker–Teter–Hutter pseudopotentials⁵¹ to describe the wave function. The system is studied in the canonical (number of atoms, volume and T) ensemble with 0.5 fs time step and 5-ps-long productive FPMD simulations. A cubic $2 \times 2 \times 2$ supercell containing 128 atoms (32 Fe, 64 O and 32 H) was fixed at lattice parameter $a=8.719 \text{ \AA}$, which corresponds to a P of 120 GPa taken from our previous FPMD simulation without an electrical field. The propagation of FPMD simulation is controlled by the optimal-sampling generalized Langevin equation thermostat⁵² with frequency centred at $3,500 \text{ cm}^{-1}$, which approximates the typical vibration frequency of the ionic O–H bond in FeO_2H_x . Systems studied at each T were equilibrated by 5 ps FPMD runs to ensure that the system is fully equilibrated before the productive run. The homogeneous static electric field was uniformly applied along the $[001]$ direction across the supercell, within periodic boundary conditions, using the Berry phase formulation⁵³.

The intensity value of the electrical field is not straightforward to determine by experiment⁵⁴. Previous experiments on water ice established a nonlinear relation between ionic voltage and current and indicated ionic current is in the microampere level in ice. The intensity of the electrical field excited by proton conduction can be estimated as follows:

$$E_{\text{IC}} = \frac{I_{\text{IC}}}{\sigma_{\text{IC}} S}$$

where I_{IC} is the ionic current, σ_{IC} is the EC related to proton condition and S refers to the lattice plane perpendicular to the direction of current in our simulation. By estimating ~ 5 – 30% of total EC coming from IC, E_{IC} is derived to be on the order of ~ 0.05 – 0.5 V \AA^{-1} . Here, we tried intensities of 0.12, 0.26 and 0.5 V \AA^{-1} as well as zero-field conditions (Fig. 2b). We found the value of 0.26 V \AA^{-1} can correctly reproduce the trend of EC in experiment. This is also a sensitive value that has previously described the electrical properties of ice I_h , ice XI^{55} and superionic $\text{H}_2\text{O}^{\text{51}}$.

Calculation of EM. The EM makes an essential contribution to the total EC, especially at relatively low T . Here we computed both e -ph and e - e contributions to the EM in superionic FeO_2H_x . We have used a dedicated method for each contribution. First, we computed the e -ph contribution on the basis of the FPMD simulations we previously conducted for FeO_2H at ~ 120 GPa and various temperatures. The contribution was calculated using the Kubo–Greenwood formula^{55,56}. At each T , 30–40 FPMD simulation snapshots were selected every 0.2 ps to maintain statistically independent atomic configurations. As averages of selected configurations with a post-processing tool, kg4vasp was implemented in VASP⁵⁷. For the electronic structure calculation, a denser k -points mesh of $2 \times 2 \times 2$ was used in the Monkhorst–Pack scheme.

We computed the e - e scattering contribution to EM using the density functional theory + dynamical mean-field theory with continuous time quantum Monte Carlo impurity solver⁵⁸ and the Kubo–Greenwood formula with the EDMFTF code⁵⁹. This method was successfully used to calculate the e - e contribution in high- P iron⁶⁰.

We sum up the separately computed e -ph and e - e contributions in the following formula, known as the Matthiessen's rule:

$$\frac{1}{\sigma_{\text{EM}}} = \frac{1}{\sigma_{e\text{-ph}}} + \frac{1}{\sigma_{e\text{-}e}}$$

The Matthiessen's rule was used in a variety of systems, including strongly correlated metals and oxides^{60,61}. The EM contribution will be finally added to the IC contribution as the total EC.

Experiment. Sample preparation. High-purity α - FeOOH powder samples are commercially available through Alfa Aesar (CAS 20344-49-4). The EC measurements were conducted in a symmetric DAC. The bevelled culet size is 150/300 μm in diameter. The Re gasket was pre-indented to 25–30 GPa, and a hole of 280 μm was drilled by laser ablation. For the EC experiment, we packed cubic boron nitride powder in the hole to isolate the four platinum (Pt) electrodes from the gasket. An α - FeOOH petite was sandwiched between two lithium fluoride layers of the thermal insulator and P medium.

Synthesis of $\text{Py-FeO}_2\text{H}_x$ using laser heating. A continuous wave ytterbium-doped fibre laser was used to heat the sample in a DAC at the Center for High Pressure Science and Technology Advanced Research (HPSTAR). The wavelength of the laser is 1,070 nm.

We applied laser heating opposite to the Pt leads such that the Pt leads were heated less to avoid Pt ion diffusion into the sample. The laser beam size (as small as 30 μm in diameter) covered the whole sample area (Extended Data Fig. 8). The T was determined by fitting the spectrum (600–800 nm at High-Pressure Collaborative Access Team (HPCAT) and HPSTAR and 700–900 nm at GeoSoilEnviroCARS (GSECARS)⁶²) with Planck radiation function using the grey-body approximation⁶³. The spectra and fitting results were reduced by t-rax software⁶⁴. The uncertainty of the

T measurement is around 100 K throughout the experiments. Using this set-up, the sample was synthesized by heating a cold-compressed goethite sample at 113 GPa and up to 2,000 K with total heating duration of approximately 1 hour. The samples were then compressed to 121 GPa, and EC measurements were performed thereafter.

High-*P* Raman spectroscopy. In situ high-*P* Raman measurements were conducted on a customized system at HPSTAR. In a separate run, we loaded goethite and Ar *P* medium in a new DAC. The Py phase was synthesized at 94 GPa and 2,200 K. Raman spectrums were collected during decompression. Spectrums were taken for the back-scattering geometry using an Argon laser (633 nm and power <1 mW) in the range 1,000–4,000 cm⁻¹ with a spectral resolution of 1.0 cm⁻¹, and the resolution of laser spot was around 10 μm. The acquiring time for each spectrum was 60 s and each collection was repeated ten times to eliminate the effects of fluorescence and cosmic rays. Raman spectra were fitted by using Peakfit v4.12 software to determine the position of each Raman mode.

The four-probe van der Pauw method. The four-probe Pt electrodes were kept separated throughout the measurement, which is seen from an extended cryogenic experiment (Extended Data Fig. 9). The initial thickness of the sample was 5.21(5) μm measured by the interferometry method. We used the equation of state of goethite, ε-FeOOH and FeO₂H₂, to estimate the in situ thickness of the sample^{16,29}. The volume collapse at the phase transition was set as 12%¹⁶. The calculation of thickness was verified by the X-ray absorption method in a separate experiment (Extended Data Fig. 8). Here, we estimate 7% error in thickness. Offline *P* was determined from the Raman spectrum of the diamond edge with an uncertainty up to 3 GPa (ref. 65). A high-precision source meter (Keithley-6212 DC current source and Keithley-2182A nanovoltmeter) was used to measure the resistance of the sample. The uncertainty from the machine is less than 0.1%. Under high *P*, the sample would no longer sustain its ideally flat condition. The roughness and unevenness of the sample relate to the paired reading from four electrodes. The total error of resistance is estimated from the difference between *R*₁₂ and *R*₃₄. The EC was calculated according to the classic van der Pauw method based on the measured resistances⁶⁶. For high-*T* EC, we applied continuous laser heating up to the highest *T*. Heating at each *T* typically stayed for 5 minutes, and resistance values were recorded and averaged over time. *T* fluctuations were within ±50 K during the entire heating cycle.

High-*P* XRD. XRD images were taken before and after EC experiments to verify the sample composition. XRD patterns are generally dominated by signature diffraction peaks from the Py phase (Extended Data Figs. 5 and 6). By calculating the lattice volumes of the Py phase, the hydrogen content *x* stayed statistically unchanged, namely from 0.87(8) before the EC experiment to 0.86(8) after the experiment. XRD experiments were conducted at both beamlines 16ID-B (sector 16) and 13ID-D (sector 13) of the Advanced Photon Source, Argonne National Laboratory and have reached consistent results. A highly monochromatized incident X-ray beam was used with a wavelength 0.4066 Å (16ID-B) and 0.3344 Å (13ID-D) and was focused down to a beam size of 5 × 8 μm and 3 × 4 μm, respectively, in the full width at half maximum.

Data availability

The data supporting the findings of this study have been deposited at the 4TU Center for Research Data (<https://doi.org/10.4121/13487643.v1>). Any additional data can be requested by e-mailing the corresponding author. Source data are provided with this paper.

Code availability

The Vienna Ab Initio Simulation Package is a proprietary software available for purchase at <https://www.vasp.at/>. CP2K is freely available under the GPL license at <https://www.cp2k.org/>. Peakfit is available for purchase at <https://sysstatsoftware.com/products/peakfit/>.

References

- Perdew, J. P., Burke, K. & Ernzerhof, M. Generalized gradient approximation made simple. *Phys. Rev. Lett.* **77**, 3865–3868 (1996).
- Kresse, G. & Furthmüller, J. Efficient iterative schemes for ab initio total-energy calculations using a plane-wave basis set. *Phys. Rev. B* **54**, 11169–11186 (1996).
- Nosé, S. A unified formulation of the constant temperature molecular dynamics methods. *J. Chem. Phys.* **81**, 511–519 (1984).
- Dickey, J. M. & Paskin, A. Computer simulation of the lattice dynamics of solids. *Phys. Rev.* **188**, 1407–1418 (1969).
- French, M., Hamel, S. & Redmer, R. Dynamical screening and ionic conductivity in water from ab initio simulations. *Phys. Rev. Lett.* **107**, 185901 (2011).
- Hutter, J., Iannuzzi, M., Schiffmann, F. & VandeVondele, J. cp2k: atomistic simulations of condensed matter systems. *Wiley Interdiscip. Rev. Comput. Mol. Sci.* **4**, 15–25 (2014).
- Goedecker, S., Teter, M. & Hutter, J. Separable dual-space Gaussian pseudopotentials. *Phys. Rev. B* **54**, 1703–1710 (1996).
- Cerioti, M., Bussi, G. & Parrinello, M. Colored-noise thermostats à la carte. *J. Chem. Theory Comput.* **6**, 1170–1180 (2010).
- Umari, P. & Pasquarello, A. Ab initio molecular dynamics in a finite homogeneous electric field. *Phys. Rev. Lett.* **89**, 157602 (2002).
- Cassone, G., Giaquinta, P. V., Saija, F. & Saitta, A. M. Effect of electric field orientation on the mechanical and electrical properties of water ices: an ab-initio study. *J. Phys. Chem. B* **118**, 12717–12724 (2014).
- Pozzo, M., Davies, C., Gubbins, D. & Alfè, D. Thermal and electrical conductivity of iron at Earth's core conditions. *Nature* **485**, 355–358 (2012).
- de Koker, N., Steinle-Neumann, G. & Vlček, V. Electrical resistivity and thermal conductivity of liquid Fe alloys at high *P* and *T*, and heat flux in Earth's core. *Proc. Natl Acad. Sci. USA* **109**, 4070–4073 (2012).
- Di Paola, C., Macheda, F., Laricchia, S., Weber, C. & Bonini, N. First-principles study of electronic transport and structural properties of Cu₁₂Sb₅S₁₃ in its high-temperature phase. *Phys. Rev. Res.* **2**, 033055 (2020).
- Hauke, K. Quantum Monte Carlo impurity solver for cluster dynamical mean-field theory and electronic structure calculations with adjustable cluster base. *Phys. Rev. B* **75**, 155113 (2007).
- Hauke, K. & Birol, T. Free energy from stationary implementation of the DFT+DMFT functional. *Phys. Rev. Lett.* **115**, 256402 (2015).
- Xu, J. et al. Thermal conductivity and electrical resistivity of solid iron at Earth's core conditions from first principles. *Phys. Rev. Lett.* **121**, 096601 (2018).
- Hausoel, A. et al. Local magnetic moments in iron and nickel at ambient and Earth's core conditions. *Nat. Commun.* **8**, 16062 (2017).
- Prakapenka, V. B. et al. Advanced flat top laser heating system for high pressure research at GSECARS: application to the melting behavior of germanium. *High Press. Res.* **28**, 225–235 (2008).
- Shen, G., Rivers, M. L., Wang, Y. & Sutton, S. R. Laser heated diamond cell system at the Advanced Photon Source for in situ X-ray measurements at high pressure and temperature. *Rev. Sci. Instrum.* **72**, 1273–1282 (2001).
- Holtgrewe, N., Greenberg, E., Prescher, C., Prakapenka, V. B. & Goncharov, A. F. Advanced integrated optical spectroscopy system for diamond anvil cell studies at GSECARS. *High Press. Res.* **39**, 457–470 (2019).
- Akahama, Y. & Kawamura, H. Pressure calibration of diamond anvil Raman gauge to 310 GPa. *J. Appl. Phys.* **100**, 043516 (2006).
- Buehler, M. G. & Thurber, W. R. An experimental study of various cross sheet resistor test structures. *J. Electrochem. Soc.* **125**, 645–650 (1978).

Acknowledgements

Y.H. is also supported by HPSTAR. We acknowledge X. Du, N. Li, Y. Zhao, W. Yang and E. Greenburg for assistance in conducting laser heating and EC measurements; J. Cheng and B. Li for conducting Raman; and Y. Sun for FPMD technical support. This work is supported by the National Key Research and Development Program of China (2019YFA0708502), the National Natural Science Foundation of China (grant no. U1530402, U1930401, 41774101 and 11774015) and the Youth Innovation Promotion Association of CAS (2020394). XRD patterns were collected at High Pressure Collaborative Access Team (16ID-B) and GeoSoilEnviroCARS (13ID-D), Advanced Photon Source (APS), Argonne National Laboratory. HPCAT operations are supported by DOE-NNSA's Office of Experimental Sciences. APS is supported by DOE-BES, under contract no. DE-AC02-06CH11357. GeoSoilEnviroCARS is supported by the National Science Foundation—Earth Sciences (EAR - 1634415) and Department of Energy—Geosciences (DE-FG02-94ER14466). M.H. is supported by NSF grant EAR-1847707. Y.Z. is supported by China Postdoctoral Science Foundation grant 18NZ021-0213-216308. J.C. acknowledges the support of NSF grant EAR-1723185. L.D. is supported by the Strategic Priority Research Program of CAS under grant XDB18000000. J.H.S. is supported by the Brain Pool Program through the National Research Foundation of Korea funded by the Ministry of Science and ICT under grant NRF-2020H1D3A2A02111022. C.J.P. is supported by a Royal Society Wolfson Research Merit Award. R.J.N. is supported by the Engineering and Physical Sciences Research Council under the grant EP/P034616/1. H.-K.M. is supported by NSF grants EAR-1722515 and EAR-1447438. Q.H. is supported by a Tencent XPLORER Prize.

Author contributions

Q.H., D.Y.K. and H.-K.M. formulated the concept of the study. Y.H., Q.H., B.G.J., J.H.S., D.Y.K., S.S., C.J.P. and R.J.N. conducted the theoretical simulation. M.H., Y.Z., L.D., F.K., B.C., J.L. and Q.H. performed electrical conductivity measurements. Q.H. carried out the Raman. J.L., Q.H., R.T., J.C., Y.M. and V.B.P. performed the XRD experiment. M.H., Y.H. and Q.H. performed the data analysis. Q.H., H.-K.M., M.H., Y.H. and J.L. wrote the manuscript with contributions from all the authors.

Competing interests

The authors declare no competing interests.

Additional information

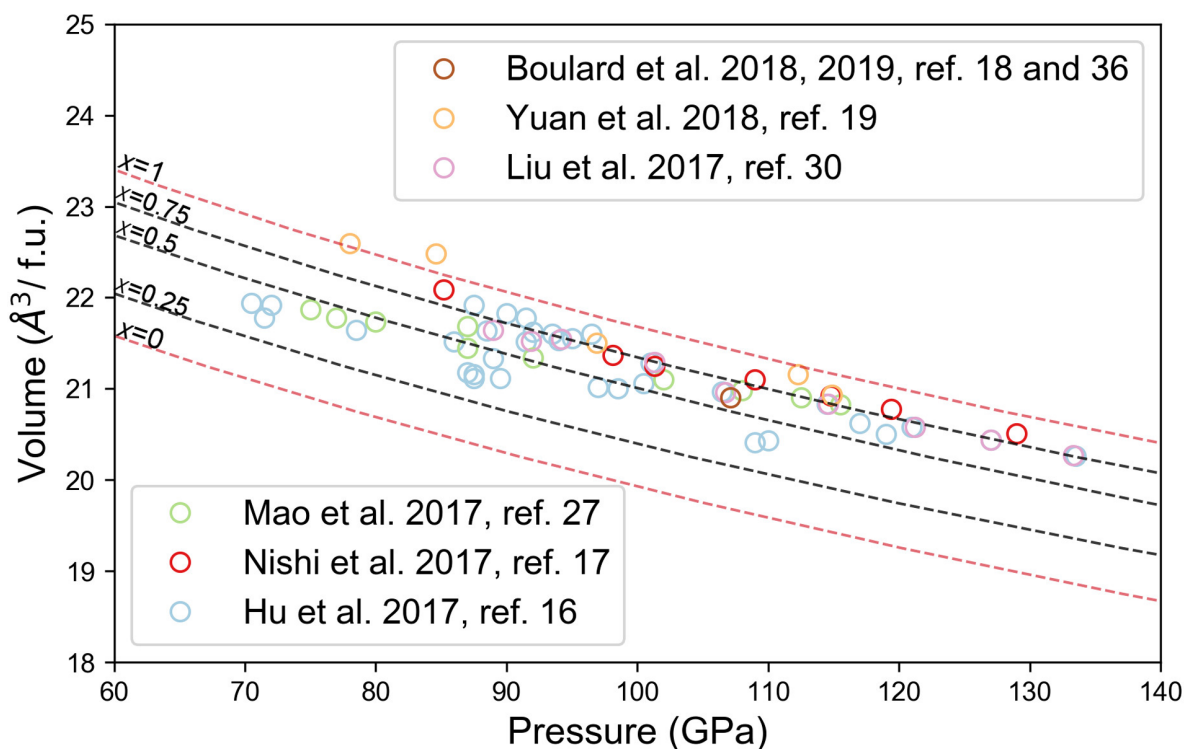
Extended data is available for this paper at <https://doi.org/10.1038/s41561-021-00696-2>.

Supplementary information The online version contains supplementary material available at <https://doi.org/10.1038/s41561-021-00696-2>.

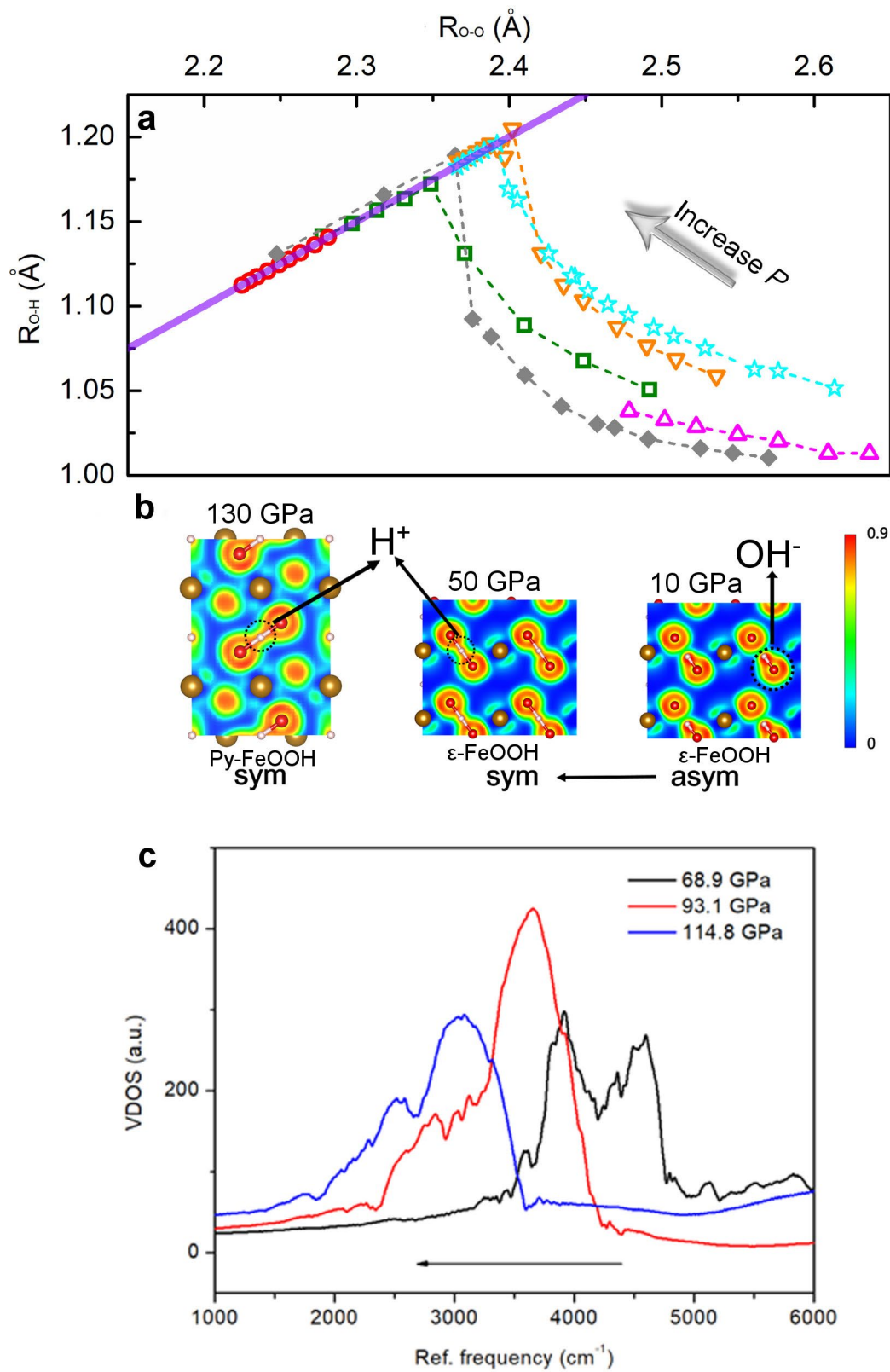
Correspondence and requests for materials should be addressed to J.L., D.Y.K. or Q.H.

Peer review information *Nature Geoscience* thanks Jean-Alexis Hernandez and the other, anonymous, reviewer(s) for their contribution to the peer review of this work. Primary Handling Editor: Rebecca Neely.

Reprints and permissions information is available at www.nature.com/reprints.

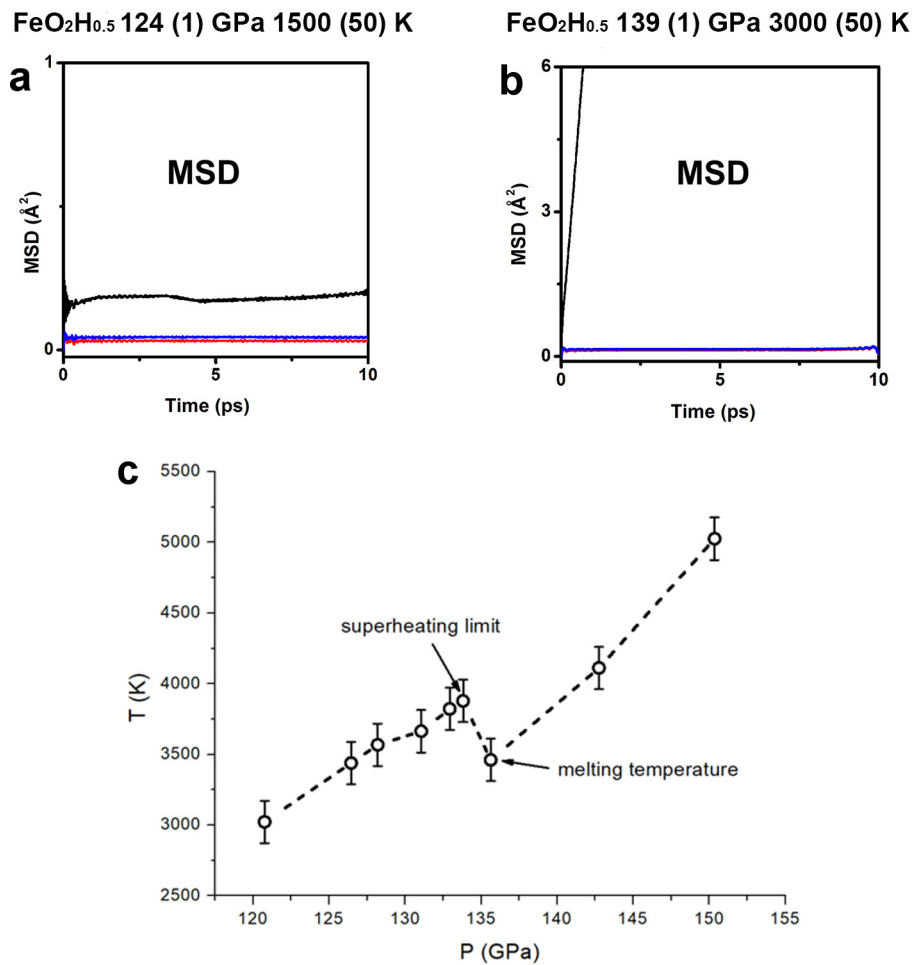


Extended Data Fig. 1 | Volumes of Py-FeO₂ and Py-FeO₂H_x under pressure and room temperature. Open circles are experimental volumes in literature. Measurement uncertainties from XRD are generally less than the symbol size. Dash curves are volumes of FeO₂H_x with $x=0, 0.25, 0.5, 0.75$ and 1.0 from theoretical calculation (see Methods). The stability and stoichiometry of FeO₂-FeO₂H in pyrite structure. In eight different experiments converting FeO₂H to the Py-phase at 86.0–133.5 GPa and 1500–2500 K, Hu *et al.* observed a wide variation of the unit-cell volume, that was attributed to the variation of x from 0.43 to 0.81 in Py-FeO₂H_x due to the difference in the P - T of their synthesis. The set of curves for the volume dependence on x and P as shown in Fig. S1. Nishi. *et al.* conducted a set of experiments with all P - V data correspond to the maximum of Hu's volume. Subsequent investigations by Yuan *et al.* from Tohoku University synthesized a Py-FeO₂H_x with unit-cell volumes 2% larger than Nishi. *et al.* approaching the full hydrogenation of $x=1$. Many additional publications in 2017–2019 further showed variation of volume and thus H. Most importantly, all experiments of four different groups consistently demonstrated that Py-FeO₂H_x ($x \leq 1$) is stable under DLM pressures and is at least thermodynamically stable up to 2500–2600 K at 110 GPa. While the exact stoichiometry of the H and its relation to P , T , and hydrogen fugacity remain interesting, it is not the subject of the present work which focuses on the superionization behavior in hydrogen in the Py phase regardless of its stoichiometry. Therefore, our FPMD simulation chose $x=0.5$ and 1.0 because they mainly cover the range of x obtained from XRD experiments.

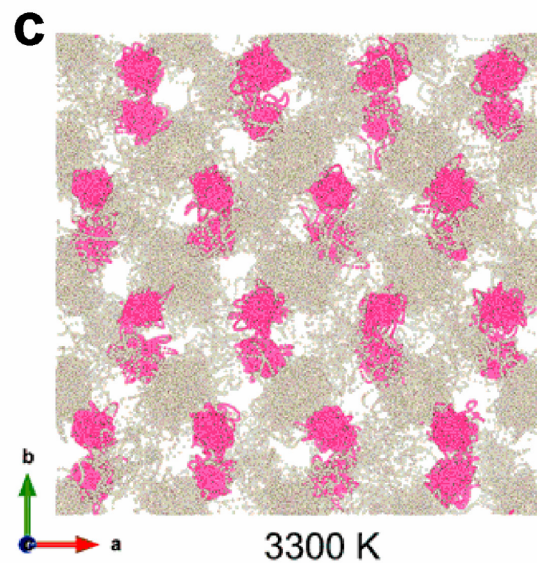
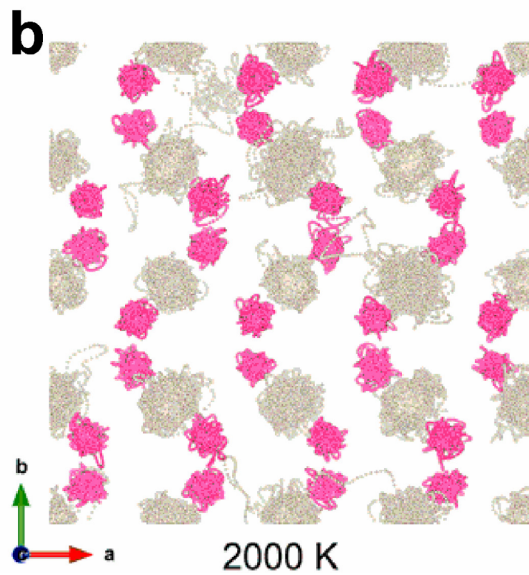
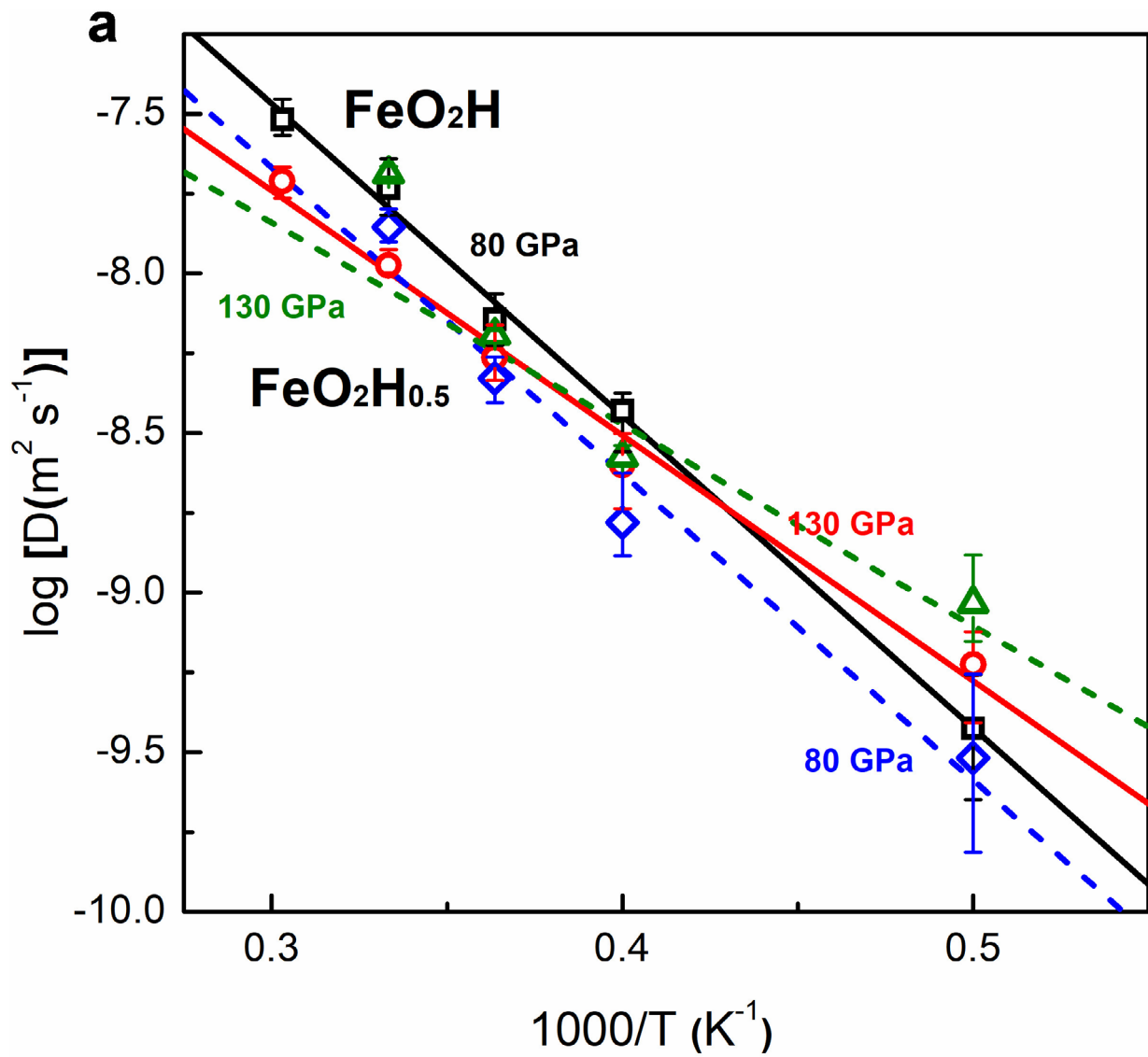


Extended Data Fig. 2 | See next page for caption.

Extended Data Fig. 2 | Covalent to ionic bonding transition. a, The evolution of $R_{\text{O-H}}$ as a function of O-O distance $R_{\text{O-O}}$. Magenta triangles: α -FeOOH; green squares: ϵ -FeOOH; red circles: pyrite FeO_2H ; orange inverted triangles: δ -AlOOH (Tsuchiya, *Geophys. Res. Lett.* 2002); cyan stars: Phase D ($\text{MgSi}_2\text{O}_2\text{H}$, Tsuchiya, *Am. Mineral.* 2005); grey diamonds: ice (VII to X) at 100 K simulated by M. Benoit *et al.* (Benoit, *Nature* 1998); purple solid line: line with symmetric O-H-O bonds ($R_{\text{O-H}} = R_{\text{O-O}}/2$). The lower panel is the electron localization function (ELF) distributions viewed along [001] direction for ϵ -FeOOH and [111] direction for Py- FeO_2H . Yellow, white, and red spheres represent Fe, H and O atoms, respectively. Once synthesized at high pressure, the Py- FeO_2H already features symmetric O-H-O bonding (Gleason *Earth Planet. Sci. Lett.* 2013). The change of $R_{\text{O-H}}/R_{\text{O-O}}$ pairs indicated the delocalization of H between the two O atoms in both ϵ -FeOOH and Py- FeO_2H when pressure raised above 50 GPa. **b**, Distribution of Electron localization function. H in the symmetric bonding partially loss its electrons and form a stronger ionic bond with O atoms. The stiffen of O-H-O bonds results in the blueshifts of hydroxyl Raman peaks (Fig. 2). **c**, Calculated VDOS of FeO_2H at 300 K and pressures of 68.9 (black curve), 93.1 (red curve), and 114.8 GPa (blue curve). The movement of vibration modes is consistent with experiment.

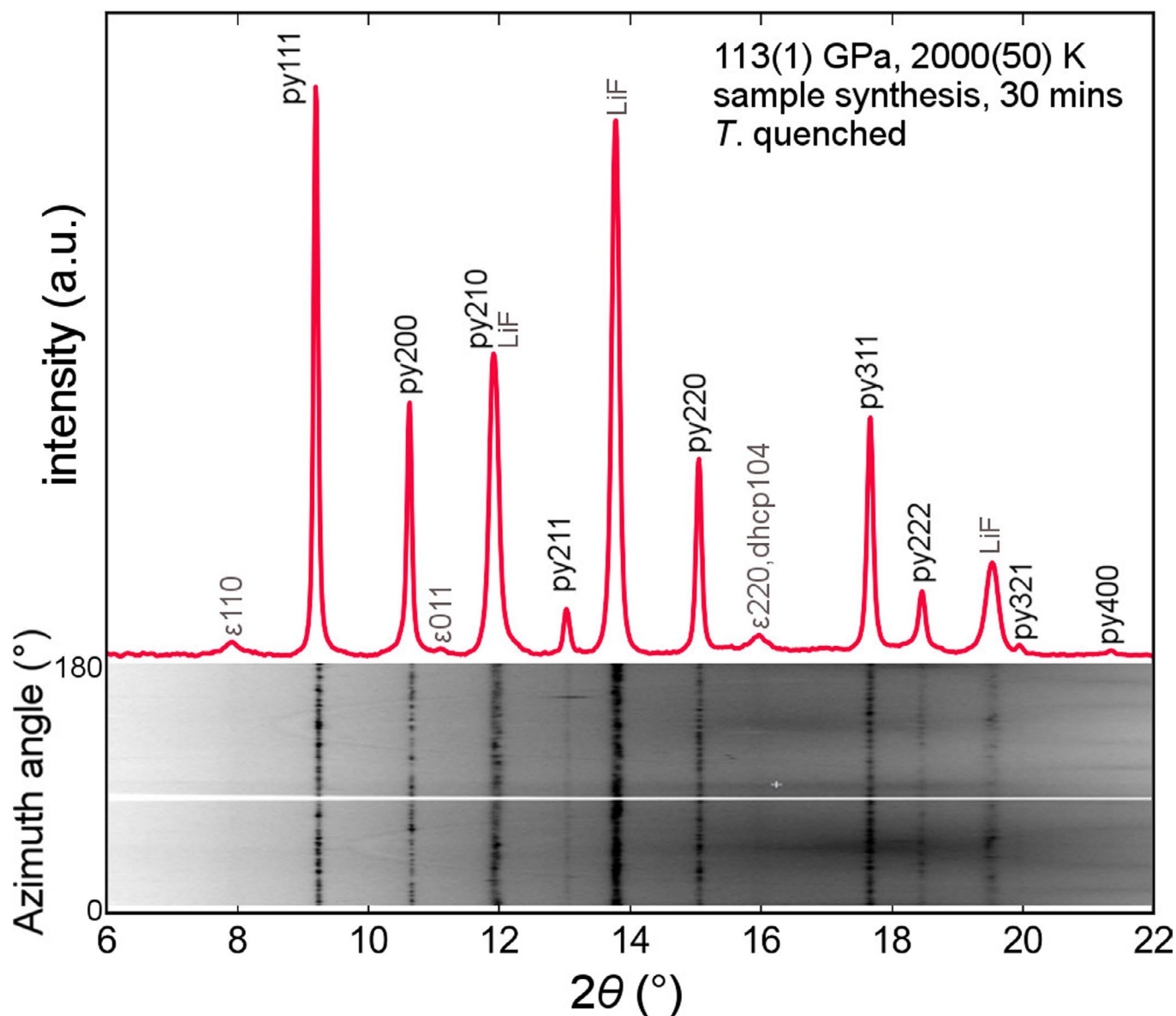


Extended Data Fig. 3 | The evolution of MSDs, trajectories and melting of $\text{FeO}_2\text{H}_{0.5}$. Black, red and blue curves represent MSDs of H, Fe and O ions in $\text{FeO}_2\text{H}_{0.5}$. **a**, Ordinary solid FeO_2H_x . **b**, The skyrocketing MSD of hydrogen indicate the onset of superionic state in Fig. 1. Uncertainties of pressure and temperature are sampled from the trajectories. **c**, Calculated melting temperature using Z method. The open circles show the pressures and temperatures of our simulations. The connection of these circles presents a shape like letter Z. The transition from the solid superheating state to liquid state is pointed out with arrows.

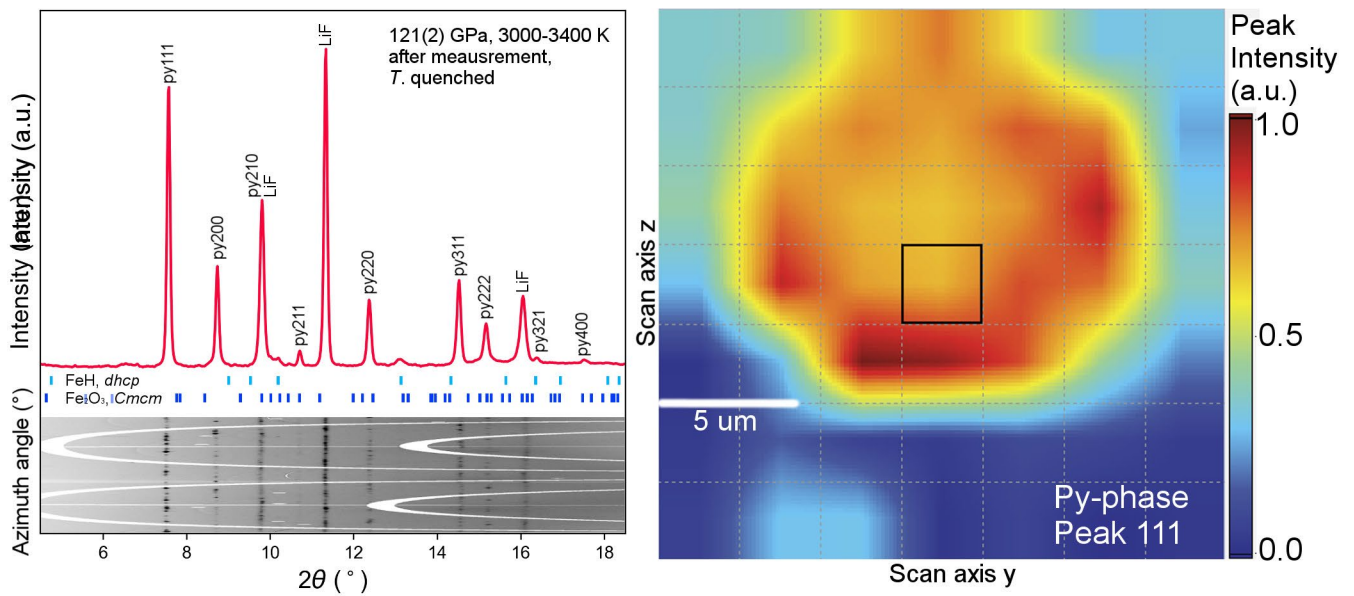


Extended Data Fig. 4 | See next page for caption.

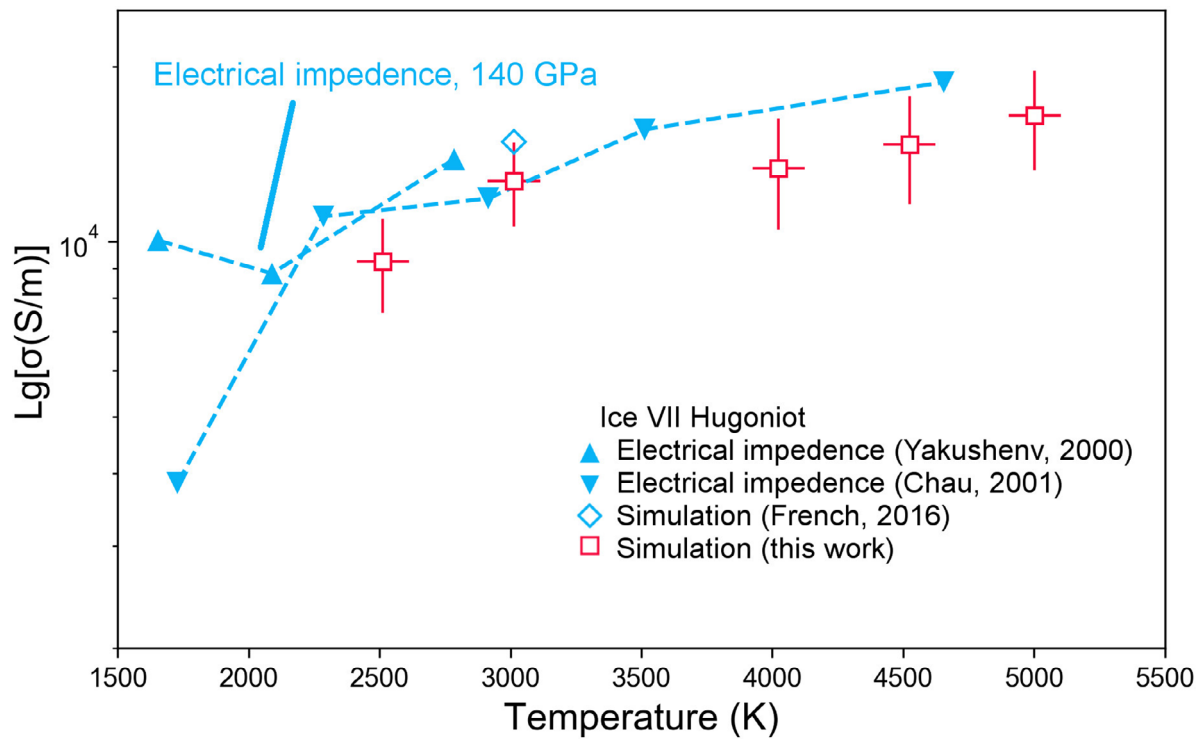
Extended Data Fig. 4 | Proton diffusion coefficients of superionic Py-FeO₂H and Py-FeO₂H_{0.5}. **a**, Black, red, blue and green symbols represent proton diffusion coefficients of FeO₂H at 80 GPa, FeO₂H at 130 GPa, FeO₂H_{0.5} at 80 GPa and FeO₂H_{0.5} at 130 GPa, respectively. **b**, The localized superionic phase with protons distributed between two nearby O ions. **c**, The delocalized superionic phase with protons delocalizing from O-H-O triplet. Small grey and pink spheres denote the trajectories of the H and O ions, respectively. The intermediate phase was previously studied by Hernandez and Caracas in ice as ice phase VII". Protons in ice VII" delocalize from the O-H-O triplet and become even more diffusive. The intermediate phase may explain the further raising of the *EC* in Py-FeO₂Hx above ~2000 K and 121 GPa. We have been inspired to conduct FPMD simulations and have also observed the delocalized phase in Py-FeO₂H at temperatures above 3000 K. We compared the trajectories of H and O ions at 2000 and 3000 K in FeO₂H. At 2000 K, the protons are mostly distributed between two nearby O ions, and they diffuse in the lattice by hopping between two symmetrized hydrogen sites. At 3300 K, movement of protons no longer binds to the nearest O atoms but travels to any possible interstitial sites in the entire lattice. The greater movement of protons can be described by the delocalized superionic phase. Similar to ice VII", this intermediate phase helps to raise the ionic conductivity from the order of 10¹-10² to above 10³ S m⁻¹ and becomes visible in *EC* experiments.



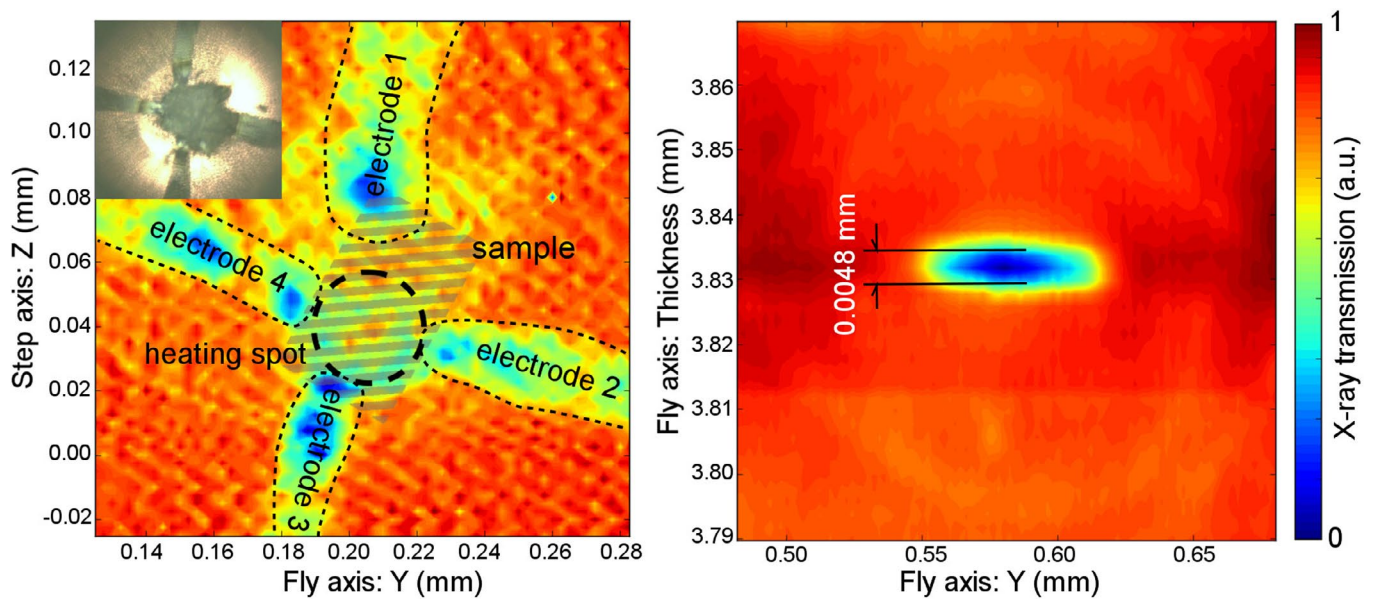
Extended Data Fig. 5 | X-ray diffraction pattern of FeO_2H_x at 113 GPa and quenched from 2000 K. Pressure is measured using the equation of state of Pt. The sample completely transformed into the Py- FeO_2H_x phase. The top panel is an integrated pattern from the 2D unrolled x-ray diffraction pattern at the bottom. The wavelength of the x-rays is 0.4066 Å. The strong diffraction peaks from the Py-phase confirmed that the majority of the sample is Py- FeO_2H_x . The lattice parameter of the Py-phase is $a = 4.392$ Å, standing for $x = 0.87(8)$ from ref.¹⁶. The remaining diffraction peaks could be indexed to the pressure medium (LiF) and very tiny amounts of ϵ - FeOOH . After heating, the pressure was equilibrated at 113 GPa and the electrical leads were checked by immersing the DAC into a liquid nitrogen cryostat. The slope of the temperature versus EC plot was positive, clearly showing four electrodes were safely connected to the non-metallic sample without a short circuit (Extended Data Fig. 9).



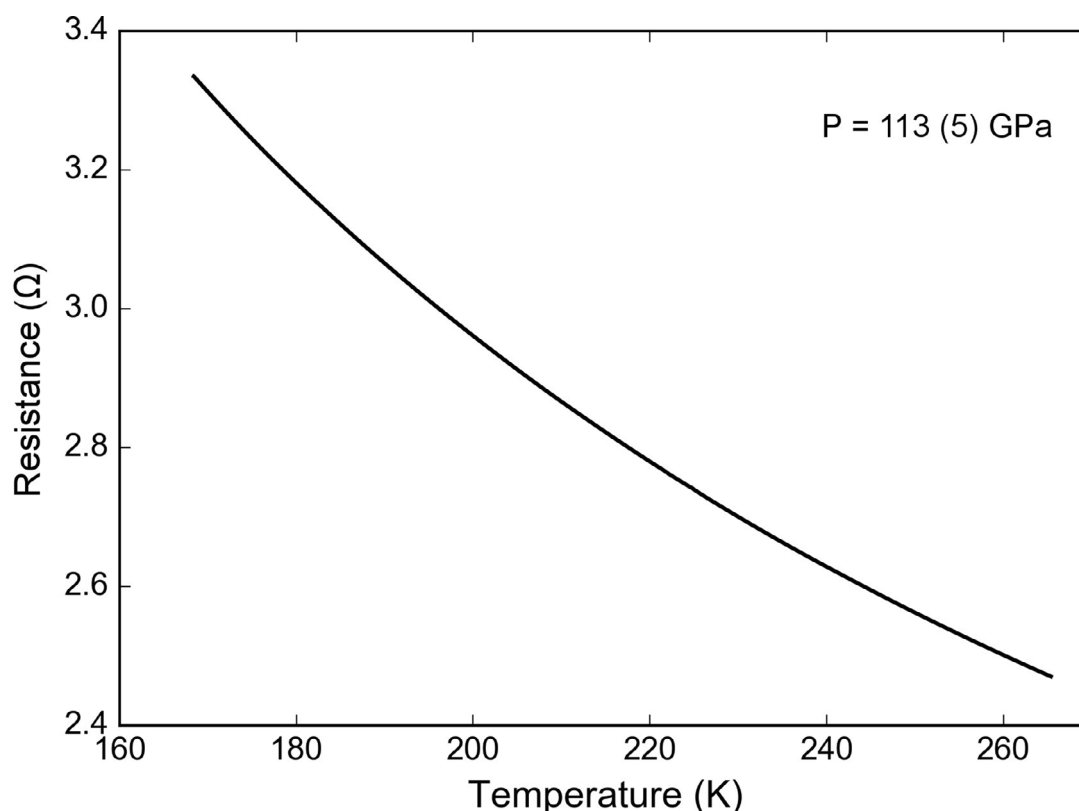
Extended Data Fig. 6 | X-ray diffraction pattern of FeO_2H_x at 121 GPa and quenched from 3000–3400 K. In the left panel, the pattern taken at the center of heating is still dominated by the Py-phase with lattice parameter $a = 4.379 \text{ \AA}$ and corresponding $x = 0.86(8)$ (ref. ¹⁶). The minor peaks in the pattern may associate with *dhcp*- FeH_x and/or *Cmcm*-type Fe_2O_3 . The reference lattices parameters are *dhcp*- FeH_x ($a = 2.458 \text{ \AA}$, $c = 8.046 \text{ \AA}$); *Cmcm*-type Fe_2O_3 ($a = 2.559 \text{ \AA}$, $a = 8.257 \text{ \AA}$, $c = 6.164 \text{ \AA}$). Pressure is measured by the equation of state of Pt. The wavelength of the x-ray is 0.3344 \AA . The right panel is an XRD mapping contour around the heating area. We first divided the heated portion of sample into $(21 \times 21 \mu\text{m}^2)$ a 7×7 matrix. We collect one XRD pattern on each grid point with the same 10-seconds' exposure time. Colors on the color bar are proportional to the intensity of Py-phase 111 peak. The contour is then constructed by interpolating those intensities.



Extended Data Fig. 7 | Electrical conductivities of superionic ice from experiments and simulations. The calculated proton conductivities of superionic ice under the P - T conditions shown in the previous figure are compared with previous experimental (Yakushenv *J. Exp. Theor.*, 2000 and Chau *J. Chem. Phys.*, 2001) and simulations (French, *Phys. Rev. Lett.* 2011).



Extended Data Fig. 8 | Image of x-ray absorption for the sample with four Pt electrodes. The sample was sandwiched by two LiF layers acting as the pressure medium and thermal isolation. Cubic-BN was used as the electrical isolator. In left panel, the shaded area corresponds to the actual sample, whose geometry was later used to determine electric conductivity. The mapping image of the x-ray absorption showed that the samples were individually connected by four Pt electrodes. The inset is the corresponding microscopic image of the sample assembly. The right panel shows the x-ray absorption along the radial side of diamond anvil cell (perpendicular to the compression axis) to access the thickness of the sample. We took this figure in a separate experiment with LiF as the pressure medium and cubic-BN isolation. Unlike the *EC* experiment, we used a Be gasket such that it is transparent to x-ray. The image was taken at 110 GPa after laser heating at 2000 K for 45 minutes. The directly measured thickness of 4.8 μm is consistent with the one we calibrated in *EC* run (4.5 μm , 113 GPa). Here, we estimate 7% of uncertainty derived from the thickness difference in these two approaches.



Extended Data Fig. 9 | Temperature versus resistance for the FeO_2H_x sample at 113 GPa. The negative T - R slope indicates that the sample is an insulator. Data points were collected every 1 second. The process of warming up from 80 K to room temperature took around 60 minutes. Systematic error for resistance is less than $10^{-3} \Omega$. We estimated 5% error in temperature, due to the temperature gradient from the thermal couple to the sample. We conducted cryogenic experiments and measured the electric conductivity of FeO_2H_x synthesized at 113 GPa. The purpose of cryogenic experiments is two-folded. First, we attempted to clarify whether FeO_2H_x is an insulator or a conductor at room temperature. Secondly, we check the connection of 4-electrode system. It is also known that compression shrinks the available space in the sample chamber. In the worst-case scenario, it might squeeze the electrodes and shorts the circuit. This would lead to a fake metallized loop. In our cryogenic experiments, the insulating nature of the sample eliminates the possibility of electrode contact contamination. These observations secured our measurements taken for the sample instead of touching the platinum electrodes. The appearance of insulating FeO_2H_x would guarantee that the van der Pauw four probe system was working. Compared with laser-heated measurements, data points collected in cryogenic experiments were controlled by a cryogenic cooling system. Two thermal couples were attached to the exterior of the diamond anvil cell and the cell was immersed in a liquid nitrogen box. The temperature was completely equilibrated around 80 K, before we removed the liquid nitrogen. The cell slowly warmed up while we measured the resistance (R) from the sample at every second. According to lattice thermal expansion of the sample, sample pressure in the cryogenic cycle is 113 ± 5 GPa.